Optical Measurements of In-flame Soot in Compression-ignited Methyl Ester Flames

Karl Oskar Pires Bjørgen,* David Robert Emberson, and Terese Løvås

Department of Energy and Process Engineering,
Norwegian University of Science and Technology, Trondheim, Norway

E-mail: karl.o.bjorgen@ntnu.no
Phone: +47 90861780

Abstract

This study investigates in-flame sooting characteristics of biodiesel surrogates in compression-ignited spray flames. The aim of the study is to produce reliable experimental data on in-flame soot for validation of kinetic mechanisms and soot models. A rapeseed oil biodiesel (RME) was compared to neat methyl oleate (MO) and methyl decanoate (MD). In addition, neat n-heptane was chosen as a baseline fuel and the effect of blending n-heptane and MD on soot production was investigated. The study was performed in a single cylinder research engine with optical access to a single spray for varying ambient gas temperatures (825 K to 990 K). The in-flame soot was measured by a high speed diffuse back-illuminated extinction imaging system, and the flame lift-off length (FLOL) and the corresponding estimated equivalence ratio at FLOL was measured from high speed OH* chemiluminescence imaging. Results show that RME has the highest tendency to soot, closely followed by MO, independent of the FLOL equivalence ratio. Having almost identical fuel properties, this is likely due to the higher degree of unsaturation in RME compared to MO. When comparing MD to n-heptane, a much lower in-flame soot production rate is observed despite the fact that MD has a higher number of carbon-carbon bonds, concluding that the high fuel oxygen ratio in MD is effectively reducing in-flame soot production. Generally, for FLOL equivalence ratio leaner than $\sim$2, no in-flame soot was produced for all ambient gas temperatures. The in-flame soot production rate also showed a clear ambient gas temperature dependence for constant FLOL equivalence ratios, where the soot production rate increased with increased gas temperatures.

Introduction

The compression ignition (CI) engine is highly relevant for research because of the higher fuel efficiency compared to the spark ignition engine. In the coming years, a low emission engine will be required in order to meet stringent regulations set by authorities. This requires a full understanding of the phenomena occurring in the combustion chamber. In particular, the production of soot in combusting fuel sprays is not fully understood.[1] An increased understanding of in-flame soot phenomena will help engine and fuel designers predict emissions of particulate matter (PM) and heat transfer due to radiation from in-flame heated soot particles.

Oxygenated fuels such as biodiesel are important to study due to the increased usage in current Diesel fuel. The European fuel standard EN590 allows Diesel fuel to contain up to 7 w% of biodiesel in commercial Diesel, and countries like China, India and Brazil intend to accelerate investments in biofuel production in the coming decade.[2] The addition of an oxygenated fuel has a large impact on the combustion process, af-

fecting the production of soot in the flame and the resulting tail pipe PM substantially. Since soot production is largely a function of chemistry, a detailed mechanism of the gas phase fuel oxidation, a numerical representation of the physical processes and a soot model are needed. Soot predictions in compression-ignited sprays based on computational fluid dynamics (CFD) simulations are currently showing discrepancies and are not well understood.[3] The development of existing soot models is still highly dependent on experiments, emphasizing the need for reliable in-flame soot measurements.

Biodiesel does not have a clearly defined molecular composition, varying based upon the feedstock. Feedstocks include oils from rapeseed, soybean, palm and sunflower. Through transesterification of the oil and an alcohol, a mixture of various alkyl esters are produced, which constitute the biodiesel fuel. The most common biodiesel consists of methyl esters produced from methanol and vegetable oils. Besides a maximum allowed content of linolenic methyl esters (12 w%) and polyunsaturated methyl esters (1 w%), the current regulation only limits the resulting physical and chemical parameters such as cetane number, boiling point, viscosity, etc., allowing the composition to vary greatly (European standard EN14214).

This variation imposes challenges to the definition of biodiesel and the fuel surrogates used in modelling. In order to reduce the calculation time of simulations, a fuel surrogate which satisfies target properties of the real fuel is chosen. The target properties of the surrogates can be C/H/O ratio, heating value, sooting tendencies, cetane number, etc. This has previously been achieved by using a single or multi-component surrogate that meets the target properties.

Existing surrogate fuel components for biodiesel consist of methyl esters of different carbon chain lengths and with varying saturation, and normal alkanes. Fisher et al. developed a detailed mechanism for methyl butanoate and methyl formate.[4] Although having a methyl ester group, methyl butanoate has a short carbon chain length of four, which was shown not to reproduce the kinetic features of the long chain methyl esters found in biodiesel (16-18 carbon atoms).[5] In order to improve the combustion characteristics, a mechanism for methyl decanoate (MD) was developed.[6] Computed results using the MD mechanism were validated with MD in a research engine, and rapeseed oil methyl esters (RME) in a jet-stirred reactor. Unlike methyl butanoate, MD was able to capture the early formation of carbon dioxide, which differentiates biodiesel fuels from Diesel fuels. Further work included adding unsaturated molecules to the surrogate fuel blend.[7] Since most of the methyl esters in biodiesel are unsaturated, adding unsaturated compounds to the MD mechanism, i.e. methyl-5-decenoate (MD5) and methyl-9-decenoate (MD9), could improve the combustion and sooting characteristics. MD9 was chosen because the double bond is located in the same position as the one in methyl oleate (MO) and as the first double bond in methyl linoleate and methyl linolenate. MD5 was chosen to highlight the effect of position of the double bond in the carbon chain. Simulations of the oxidation of the ternary surrogate blend of n-heptane, MD and MD9 were compared to experiments of RME under diesel-like conditions in a jet-stirred reactor (JSR)[8] and showed good global agreement. In 2011, Westbrook et al. presented a detailed mechanism for longer methyl esters.[9] The mechanism includes the five major components of biodiesel: methyl stearate, methyl oleate, methyl linoleate, methyl linolenate and methyl palmitate, being able to mimic a real biodiesel with different compositions.

MD has previously been studied optically in optical engines and combustion vessels at numerous occasions.[10–14] This is mainly because it has proven to be a fitting surrogate fuel for biodiesel, but also because it produces small amounts of in-flame soot due to a high oxygen content, making it suitable for certain measurement techniques which require low in-flame soot. The interest in oxygenated fuels is mainly driven by the reduced in-flame soot and possibly reduced PM. Using oxygenated fuels has shown to facilitate the concept of leaner lifted-flame combustion (LLFC),[12,15] where the aim is to produce non-sooting, mixing-controlled flames in CI engines in order to eliminate PM

engine out emissions.

An investigation of MD and Diesel fuel combustion in an optical direct injection (DI) engine was conducted by Cheng et al.[11] MD was shown to produce very small amounts of in-flame soot compared to Diesel fuel, although having similar flame lift-off lengths (FLOL) during mixing-controlled combustion. The calculated equivalence ratio at flame lift-off location was significantly lower for MD compared to Diesel, which likely explains the low level of in-flame soot.

Several oxygenated fuels and blends were tested in a constant-volume vessel by Manin et al.,[10] where the FLOL and in-flame soot were measured. They concluded that the total in-flame soot mass produced is inversely proportional to the oxygen content of the fuel. In addition, the comparison between a tripropylene glycol monomethyl ether (TPGME)-alkane blend and MD, both having similar oxygen contents (measured by fuel oxygen ratio), showed that the location of the oxygen atoms in the molecule is important for the in-flame soot, where the TPGME-alkane blend yielded the lowest in-flame soot level. Also, for a given ignition delay time (IDT), FLOL tended to increase with addition of oxygen to the fuel, which also supports the statement of IDT and FLOL not being one-to-one correlated.[16]

In order to investigate the effect of molecular structure on soot processes in spray combustion, numerical simulations for several oxygenated fuels and blends (including MD) were performed by Park et al.[17] Soot precursors (acetylene) in the spray combustion were shown to decrease with increased fuel oxygen ratio and decreased number of carbon-carbon bonds in the molecule. The soot formation for fuel blends with similar fuel oxygen ratio and number of C-C bonds was mainly governed by the IDT and the FLOL. This study also highlighted that in-flame soot production is highly dependent on the molecular structure, as well as the fuel-air mixing.

A comparison between a long and a short carbon-chain biodiesel was conducted in a small bore engine by Zhang et al.[18] They concluded that an increase in carbon chain length leads to reduced IDTs for the long chain biodiesel, increasing the mixing controlled burn phase duration. The long chain biodiesel produces more soot due to less premixing and a lower fuel oxygen content.

The authors have not found any previous studies conducting optical measurement of in-flame soot for longer chain neat methyl esters such as MO. In this study, the combustion of a commercial RME, neat MO, neat MD, neat n-heptane and a 50 % molar blend of MD and n-heptane have been investigated for varying ambient gas temperature conditions. MO is chosen because of the large content of it in RME, making the data valuable for future validation of CFD and kinetic simulations of RME. Also, by comparing MO to RME, the observed difference will be attributed to the remaining components in RME. MD (neat or blended with an alkane) is a widely used surrogate fuel for biodiesel. The aim is to compare combustion and in-flame soot characteristics of a real biodiesel to possible surrogate fuels under engine-like conditions, and to examine the effect of fuel-bound oxygen and degree of unsaturation on these characteristics.

Methods

Optical Accessible Compression Ignited Chamber

The experiments were performed in the Optical Accessible Compression Ignited Chamber (OACIC) at the Department of Energy and Process Engineering at the Norwegian University of Science and Technology (NTNU). The OACIC is a modified four-stroke engine (Lister 12 CS) where the head has been redesigned for optical access. The combustion chamber located in the head is connected to the engine's swept volume via an interchangeable throat (Figure 1). A second-generation Bosch solenoid common rail injector is installed in the chamber, fitted with a single hole nozzle having an angle of 62° degrees with respect to the nozzle axis. The intake and exhaust valves are taken from the original engine and are installed in the head. The OACIC is only lubricated with light

lubricants, to avoid any PM emissions associated with engine oil. A summary of engine dimensions and details are given in Table 1.

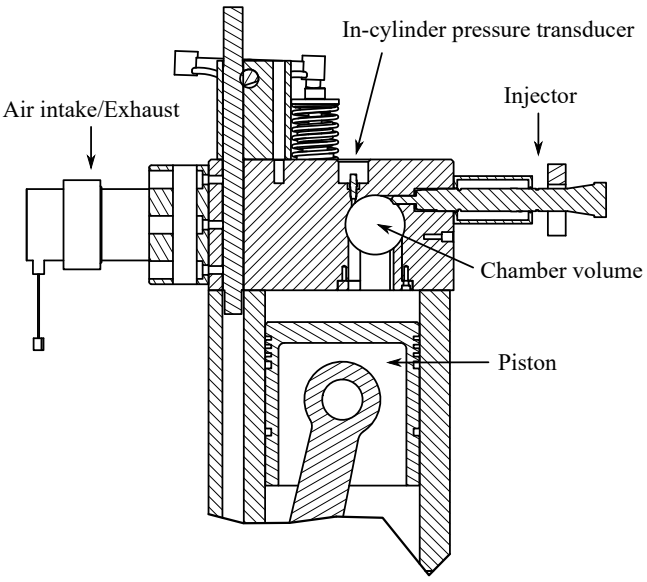

Figure 1: Cross-section of the OACIC.

Table 1: Engine specifications of the OACIC.

Engine type	4-stroke, single-cylinder, indirect DI engine
Bore/Stroke	130 mm/140 mm
Displaced volume	1.85 l
Compression ratio	15.9
Injector	Bosch CR 2nd gen
Injector nozzle	Single hole, DSLA124P1659 62° wrt. central axis
Hole diameter	0.12 mm
Injection pressure	1000 bar
Injection duration	4.48 ms
Injection timing	2.7° before TDC

The combustion chamber is cylindrical in shape with a diameter of 50 mm and 40 mm deep, sealed with two fused-silica windows (63 mm in diameter and 25 mm thick) and copper gaskets. The windows allow a line-of-sight view of the chamber and are retained by two threaded rings.

The piston and crank are driven by an AC motor operated at 500 rpm. The position of the crank shaft is measured by a magnetic shaft encoder, with 3200 readings per revolution, resulting in 0.1125 crank angle degrees (CAD) cycle resolution (37.5 μs time resolution for 500 rpm). A dynamic pressure sensor (Kistler 6052C) synchronized with the shaft encoder records motored and combustion pressures in the chamber.

Fuel System

The injection pressure is driven by an air-driven pump. The injections are controlled by an injection driver (National Instruments Drivven) through Labview and only triggered when the injection pressure is within ±10 bar during a cycle, resulting in a standard deviation of 2% of the target pressure. The total volume of the fuel system is kept to a minimum in order to minimize waste of fuel. A minimum volume of ∼200 ml fuel for a complete fuel measurement was required. The injector is water-cooled by a cooling jacket fitted around the injector body.

Intake Air and Exhaust System

The intake air system consists of a large air box with an orifice plate for measuring the volume flow rate of the intake air. The intake air is then compressed by a roots compressor coupled to a settling tank to dampen pressure oscillations before the OACIC. A 2 kW electric flow heater is installed near the intake manifold, heating the air up a maximum of ∼150°C. The inlet air temperature is measured by a K-type thermocouple, the inlet air pressure is measured by a high speed absolute pressure sensor (Kistler 6011), located close to the inlet manifold. The temperature of the exhaust gases are also measured by a K-type thermocouple.

Thermal Conditions

The thermal conditions of the OACIC have been assessed by measuring the temperature during motoring under several conditions. The cylinder is constantly kept at 90°C by heaters, whilst the head is neither externally cooled nor heated. A K-type thermocouple is installed in the head located 21 mm from the combustion chamber wall, giving an indication of the

head temperature. Additionally, a measurement performed using a stripped injector installed with a thermocouple in the centre axis allowed for measurement of the nozzle tip temperature during motoring. The injector tip temperature reached ∼160°C during stable operation of the OACIC. During ordinary operation of the OACIC for optical measurements, skip-fire mode was enabled with a minimum of 10 motored cycles before each combustion cycle, ensuring that the thermal conditions are more stable during the operating period. This also ensures that no post-combustion gases from the previous combustion cycles are present in the chamber during measurement.

Thermodynamic Analysis

The in-cylinder gas pressure is a common measurement in engine research and is considered a highly reliable measurement. However, the in-cylinder gas temperature is a much harder quantity to measure. In this study, an estimation of the in-cylinder ambient gas temperature was made, involving a combination of in-cylinder pressure measurements and a thermodynamic model available in the commercial software LOGEresearch by LOGE AB.

A zero-dimensional analysis of the thermodynamic conditions in the chamber has been made using a first law approach. The inputs to the calculation were absolute inlet air pressure, inlet air temperature, engine dimensions, wall temperature and in-cylinder gas pressure. The in-cylinder gas temperature is iteratively calculated based on the energy conservation equation and ideal gas law, and the heat transfer is modelled by the Woschni correlation.[19] The model also takes into account the temperature dependence of the gas properties.

Several motored pressures with varying inlet conditions were acquired and compared to the modelled pressure. Since the modelled pressure did not include blowby, the modelled pressure yielded a higher in-cylinder pressure. Mass loss due to blowby was accounted for by decreasing the compression ratio in the model, such that the measurements matched the modelled pressure. This obviously did not give the correct total mass in the chamber, but yielded a good estimation of the in-cylinder temperature and density. Consistency of the blowby for the entire range of conditions in the OACIC was checked by repeating this for all measured conditions in the OACIC, resulting the same reduced compression ratio for all conditions. The reduced compression ratio was found to be 12.6 (geometrical CR = 15.9).

Four thermodynamic conditions were chosen in this study. The ambient gas density was kept constant at ∼16.6 kg/m^3 for all conditions, whilst the ambient gas temperature was varied. The conditions are given in Table 2,

Table 2: Calculated average thermodynamic conditions of the ambient gas in the OACIC, based on combustion of all fuels. ρ_{TDC}, P_{TDC} and T_{TDC} is density, pressure and temperature of the ambient gas (respectively) at top dead center (TDC) during motoring of the OACIC. T_{max} and T_{span} is the maximum ambient gas temperature and the temperature span during the fuel injection period (with combustion), respectively. Temperature span is defined as the difference between the maximum and minimum ambient gas temperature during the injection period.

Condition	1	2	3	4
ρ_{TDC} $[kg/m^3]$	16.7	16.7	16.6	16.6
P_{TDC} $[bar]$	39.7	42.1	44.4	46.7
T_{TDC} $[K]$	825	877	928	978
T_{max} $[K]$	837	890	941	990
T_{span} $[K]$	12	13	13	12

The temperature distribution near TDC in the chamber is heterogeneous, mainly due to cooling of the gas near the chamber walls. Since the fuel spray is directed towards the center of the chamber, the center gas temperature, which is less affected by the wall cooling, is a more relevant measure to consider as the entrained gas temperature between start of injection and start of combustion.

During combustion in the chamber, the pressure increases above the motored pressure due to local heat release in the spray combustion,

expanding the combusting gases. The expansion causes the air in the chamber to compress, increasing the ambient gas temperature. The increase in temperature due the combustion was estimated from the in-cylinder combustion pressure. Adiabatic compression of the non-reacting air was assumed and the temperature increase was calculated based on numerical integration of

$$\frac{dT}{dt} = \frac{R \cdot T}{c_p(T) \cdot P} \cdot \frac{dP}{dt}, \quad (1)$$

with air being the compressed medium, R is the specific gas constant, c_p is the temperature dependent specific heat capacity for constant pressure. The initial temperature used in the calculation is taken from the motored ambient gas temperature mentioned above at the start of combustion. Results of the average ambient gas temperature during combustion for all conditions and fuels are shown in Figure 2. The ambient gas temperature variation over the period of injection is relatively stable, varying by $\sim$12 K for all conditions.

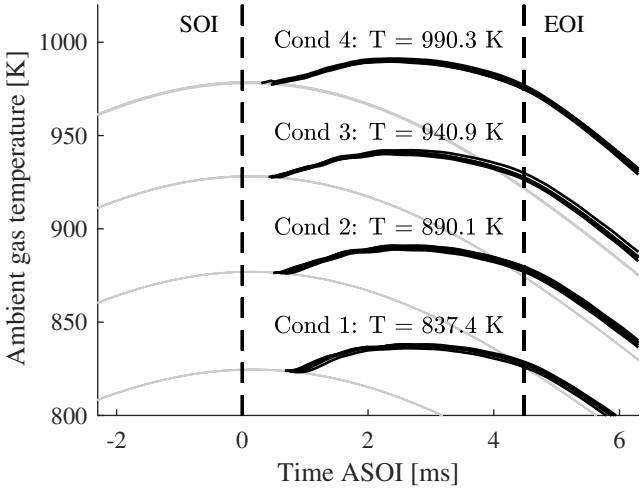

Figure 2: Estimated average ambient gas temperature in the chamber during motored and combustion cycles for all fuels and conditions. Maximum temperature (T_{max}) during the injection period, start of injection (SOI) and end of injection (EOI) are indicated.

Fuels

The dominating component in the current RME fuel is the unsaturated ester MO (see Table 3) with 61.8 w%, followed by methyl linoleate with 18.4%. Important physical and chemical properties are listed in Table 4 for all fuels. MD had a purity of $\geq$99% and the MO 96%.

Table 3: Molecular composition of the rapeseed oil methyl ester (RME).

Component	w%
Methyl oleate (C18:1)	61.8
Methyl linoleate (C18:2)	18.4
Methyl linolenate (C18:3)	7.3
Methyl palmitate (C16:0)	4.4
Methyl stearate (C18:0)	1.6
Other	6.5

As RME contains a large portion of MO, their properties should be similar, which is confirmed in Table 4. The second and third largest components in RME are methyl linoleate and methyl linolenate, where the degree of unsaturation of these molecules are 3 and 4, respectively. This is the reason for RME having a 10% higher degree of unsaturation compared to MO. An increase in level of unsaturation of neat methyl esters is known to decrease the cetane number, the kinematic viscosity, heat of combustion and melting point.[20] In addition, the C/H/O ratios of RME and MO are very similar, resulting in a similar fuel oxygen ratio (Ω_f). The calculated fuel oxygen ratio Ω_f is defined as the ratio between the oxygen present in the fuel and the amount of oxygen needed to convert all carbon and hydrogen in the fuel molecule into carbondioxide and water,[21]

$$\Omega_f = \frac{n_O}{2n_C + 0.5n_H} \quad (2)$$

where n_O, n_C and n_H is the number of oxygen, carbon and hydrogen atoms in the fuel molecule. MD is a shorter chain methyl ester compared to RME and MO, resulting in some properties being completely different. The main difference is the much higher fuel oxygen

ratio of 6.06, compared to ∼3.60 of the long chain methyl esters. Moreover, the combined effect of a lower degree of unsaturation, oxygen content and number of C-C bonds results in MD having a much lower expected tendency to produce soot compared to the longer chain methyl esters.[17,22] The main similarities between MD and RME/MO are the density and the lower heating value, resulting in similar total energy injected when using the same injection strategy.

The choice of including neat n-heptane to this study is mainly motivated by having a baseline fuel which is thoroughly investigated previously and which is commonly used as a component in biodiesel surrogates. The 50% molar blend of n-heptane and methyl decanoate (HP-MD) will highlight the effects on soot production when changing some key properties such as fuel oxygen ratio, number of C-C bonds and degree of unsaturation.

Diffuse Back-illuminated Extinction Imaging of Soot

For measuring in-flame soot, diffuse back-illuminated extinction imaging (DBIEI) was used. DBIEI is a non-intrusive two-dimensional line-of-sight measurement, where the principle of light extinction is applied, which occurs when light is either absorbed or scattered by soot particles present in the light path. The optical depth of the soot particle cloud can be calculated from the Beer-Lambert law,[33] where the transmittance τ, being the ratio between the incident light intensity I_0 and the transmitted light intensity I_t, can be related to the optical depth KL as

$$\tau = \frac{I_t}{I_0} = exp\left(-\int_L k(x)dx\right) = e^{-KL} \qquad (3)$$

where, $k(x)$ is the local dimensional extinction coefficient, x is the spatial position along the light path. K is defined as the path-averaged dimensional extinction coefficient, L is the path length through the soot particle cloud and the product KL is the observed optical depth of the soot particle cloud in a line-of-sight light extinction measurement.

The measured optical depth KL can be related to the soot volume fraction[34] f_v by

$$f_v = \frac{\lambda K}{k_e}, \qquad (4)$$

where k_e is the non-dimensional extinction coefficient and can be described as $k_e = 6\pi E(m)(1+\alpha_{sa})$. $E(m)$ is the imaginary part of the refractive index function (m being the complex refractive index of the soot particles), whilst α_{sa} is the scattering-to-absorption ratio in the measurement (calculated from RDG-FA theory). α_{sa} is known to be non-constant mainly dependent on the size of the particles, but often assumed as close to zero for spray combustion. Values of $E(m)$ and α_{sa} recommended by Engine Combustion Network (ECN)[35] for the incident light source wavelength of 628 nm are chosen for the quasi-steady period of the high-pressure spray combustion for all fuels tested, $k_e = 7.2$. The assigned uncertainty of k_e is ±20%. The quasi-steady period for the current study will be defined later.

Optical Setup

A detailed description of the DBIEI setup used in the current study is thoroughly described by Bjørgen et al.,[36] and is similar to setups used by Pastor et al.[37] and Skeen and Yasutomi.[38]

As shown in Figure 3, a high power LED with wavelength of 628 nm (FWHM = 15 nm) was used as the back-illumination light source for the DBIEI. The light from the LED is directed on to an engineered diffuser (spreading angle of 15 degrees) and further directed through the chamber volume. The angular distribution from the diffuser is measured to have a uniform intensity distribution across over the specified 15 degrees. The setup is designed according to the recommended criteria described by Westlye et al.[39] for complete abatement of beam steering effects, due to large density gradients normally present in high pressure spray combustion.

The LED is pulsed by an in-house built driver, enabling short and high power light pulses. The light pulses are synchronized with every

Table 4: Physical and chemical properties of rape seed oil methyl ester (RME), methyl decanoate (MD), methyl oleate (MO), n-heptane and a 50% molar blend of n-heptane and methyl decanoate (HP-MD).

	Unit	RME	MD	MO	N-heptane	HP-MD
Lower heating value	$[MJ/kg]$	37.82[a]	36.7	40.1[f]	44.6[g]	-
Carbon	$[w\%]$	0.771	0.709	0.770	0.839	0.755
Hydrogen	$[w\%]$	0.121	0.119	0.122	0.161	0.134
Oxygen	$[w\%]$	0.109	0.172	0.108	0.000	0.112
Fuel oxygen ratio Ω_f[j]	$[mol\%]$	3.62	6.06	3.57	0.00	3.01
Density at 15 °C	$[g/ml]$	0.8833[a]	0.8728	0.8704	0.6880[g]	-
Viscosity at 40 °C	$[mm^2/s]$	4.434[a]	1.72[e]	4.51[e]	0.34[i]	-
Cetane number	$[-]$	57.1[a]	47.9[c]	57[b]	56[d]	-
Derived Cetane number	$[-]$	-	51.6[f]	59.3[k]	53[l]	-
Normal boiling point	$[°C]$	350.2[a]	225[b]	350[b]	98.52[h]	-
Degree of unsaturation	$[mol^{-1}]$	2.21	1	2	0	0.5
Number of C-C bonds	$[\#/mol]$	16.9	9	17	6	7.5

[a] Measured [b] Ref. 23 [c] Ref. 24 [d] Ref. 25 [e] Ref. 26 [f] Ref. 27 [g] Ref. 28 [h] Ref. 29 [i] Ref. 30 [j] Ref. 21 [k] Ref. 31 [l] Ref. 32

second exposure of the main high speed camera, enabling an alternating measurement of the transmitted intensity distribution I_{tf} (LED and flame luminosity superimposed) and the flame luminosity intensity distribution I_f (flame luminosity only). A second high speed camera with equal optics, measuring the same field of view as the main camera through a 50/50 visible light beam splitter, is synchronized with the main camera. However, the second camera is given a small time shift such that it does not overlap with the light pulses. This ensures that the second camera is measuring I_f shortly before the I_{tf} measurement. The information obtained from the second camera is then used to correct for the flame luminosity effects on the main camera, giving the true transmitted intensity distribution $I_t = I_{tf} - I_f$.

Both high speed cameras used were Photron FASTCAM SA5, fitted with Nikkor 50 mm f/1.2 objective lenses and 500D close-up lenses. The spectral filters used were centred at 634 nm (FWHM 70 nm) and neutral density filters were used for adjusting the light intensity such that the measurement was close to the saturation limit of the cameras, maximizing the dynamic range of the measurement. All measurements were recorded at 100 kfps, with 1 μs exposure time and a resolution of 320x192, where the pixel scale was 0.16 mm/px.

OH* Chemiluminescence Imaging

In addition to measuring in-flame soot distribution, instantaneous natural luminosity of the flame in the UV wavelength range was measured simultaneous. This spectral interval is known to be dominated by chemiluminescence from short-lived exited-state OH (OH*), indicative of high temperature and stoichiometric combustion conditions in the flame.[40] A high speed measurement of the OH* distribution gives a measure of when and where high temperature combustion starts, and the instantaneous FLOL. The latter is as previously mentioned closely related to in-flame soot formation.[41]

The OH* distribution was measured using a Lambert Instruments gated intensifier (II25) fitted on to a Photron FASTCAM SA-X2. A UV 100 mm f/2.8 CERCO 2178 lens from Sodern fitted with a spectral filter centred at 307 nm (FWHM 10 nm) was used. The measurement was synchronized to half the speed of the DBIEI cameras, i.e. 50 kfps, in order to match the light extinction measurement frame

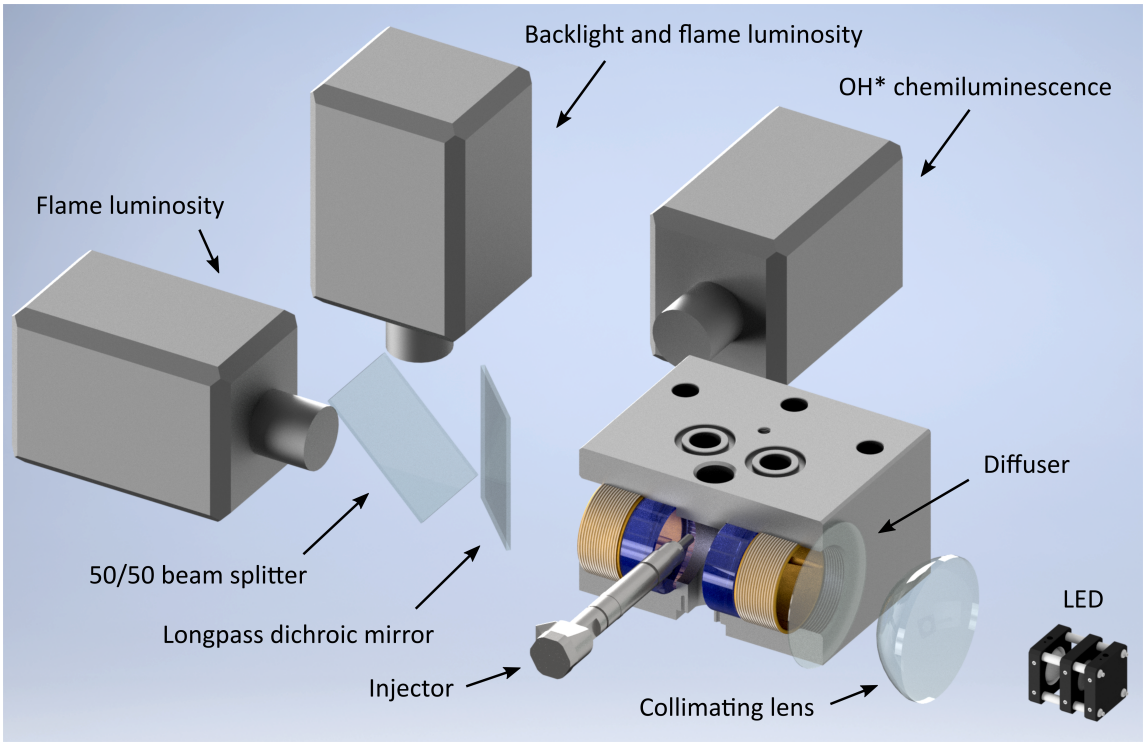

Figure 3: Optical setup. Components from right to left: 628 nm LED with focusing lenses, collimating lens (focal length 100 mm, diameter 100 mm), engineered diffuser (divergence angle 15°, diameter 100 mm), longpass dichroic mirror (cut-on wavelength 480 nm) and 50/50 visible light beam splitter.

rate. The gating time of the intensifier was set to 5 μs and centred to the DBIEI main camera exposure position. The resolution of the camera was 256x256, with a pixel scale of 0.215 mm/px. The same field of view as the DBIEI setup was captured by using a dichroic mirror, reflecting light with shorter wavelength than 480 nm and transmitting longer wavelengths to the DBIEI measurement setup.

Analysis of OH* Chemiluminescence

The FLOL was defined as the distance along the central axis between the nozzle orifice and location where the OH* chemiluminescence reached 50% of a predefined threshold value. The characteristic OH* intensity value was defined as where the OH* signal levelled off after the initial steep increase, denoted as the OH* signal shoulder value in Figure 4. The pixel intensities during the quasi-steady period did not saturate. Since the OH* signal slope at the location of the FLOL is relatively large, the determination of the shoulder value did not affect the FLOL greatly.

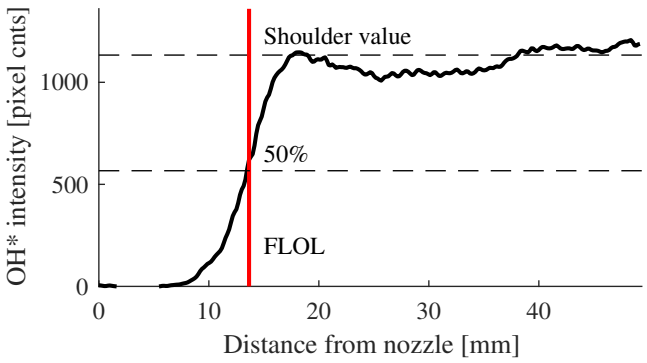

Figure 4: OH* intensity plotted along the central axis together with the definition of FLOL.

Steady FLOL

Having measured the instantaneous OH* distribution for 10 injections over 3 runs, an average of 30 injections could be used to determine the FLOL for all conditions and fuels. Also, by

identifying the period where the flame is fully developed, also known as the quasi-steady period, i.e. during the mixing controlled combustion phase, after the premixed combustion phase and before end of injection, a total of 2730 images per fuel and condition were used for the ensemble-averaged OH* image.

Equivalence Ratio at Flame Lift-off Location

The FLOL indicates the amount air that has been entrained in the fuel spray prior to combustion. A shorter FLOL indicates less entrained air and vice versa. In order to assess the sooting characteristics between the fuels and conditions, the equivalence ratio at the flame lift-off location is needed. A model for a non-reacting spray was used for assessment of the equivalence ratio at flame lift-off location.[42,43] The model is assumed to be valid for the current measurements since no combustion occurs upstream of the flame lift-off location. The cross-sectional average equivalence ratio at flame lift-off location is given by

$$\bar{\phi}(H) = \frac{2(A/F)_{st}}{\sqrt{1+16(H/x^{+})^{2}}-1}, \qquad (5)$$

where H is the FLOL, $(A/F)_{st}$ is the stoichiometric air-fuel ratio by mass and x^{+} is the characteristic length scale,

$$x^{+} = \sqrt{\frac{\rho_f}{\rho_a}}\frac{\sqrt{C_a}\cdot d}{tan(\theta/2)\cdot a}, \qquad (6)$$

where ρ_f is the density of the fuel, ρ_a is the ambient gas density, C_a is the area contraction coefficient, d is nozzle diameter, a is a constant equal to 0.75,[44] $\theta/2$ is the half spreading angle of the spray. A value of 0.85 was chosen as the C_a based on measurements of various nozzles in Ref. 43. The nozzle diameter was $d = 0.12$ mm. The primary effect on the spreading angle is shown to be the ambient gas/fuel density ratio[43] (ρ_a/ρ_f). The calculation of $\bar{\phi}(H)$ was not performed with intention of evaluating the absolute value, but rather to investigate trends.

As the ambient gas density in this study is kept constant at 16.6 kg/m^3, only the fuel density is changing between the tests. Since the fuel density for RME, MD and MO are relatively similar, the spreading angle for the sprays under all conditions tested is expected to be similar. This means that $\bar{\phi}(H)$ is mainly sensitive to changes in $(A/F)_{st}$ and H. The spreading angle is therefore calculated using an empirical relation only considering ambient gas/fuel density ratio from Ref. 43. Note that heptane and the MD-heptane blend have much lower fuel density than the neat methyl esters, making the comparison between these more uncertain.

Analysis of In-flame Soot

Total Soot Mass

The in-flame soot measured by the DBIEI can be evaluated in several ways. The line-of-sight measurement of KL provides a measure of the total soot mass within the collection cone of a pixel on the camera sensor. Based on Equation 4, and assuming that the angle of the collection cone in the DBIEI setup is small, the total mass of soot present in the collection cone of the objective lens is given by

$$m_{soot} = \rho_{soot}\frac{\lambda\cdot KL}{k_e}\cdot\Delta A_{px} \qquad (7)$$

where ρ_{soot} is the density of soot and ΔA_{px} is the projected pixel area in the focal plane. In this calculation, the uncertainty from k_e (as discussed earlier) and ρ_{soot} must be combined. Values for ρ_{soot} found in literature ranges from 1.12 g/cm^3 to 1.8 g/cm^3.[45,46] The chosen value of soot density in this study was 1.8 g/cm^3, since this is most commonly reported for in-flame Diesel combustion. Due to restriction from the combustion chamber geometry, the entire flame is not measured by the DBIEI during the quasi steady period. Hence the total soot mass is only captured during the premixed combustion stage, where the entire flame measured. By applying this method to the premixed burn phase, the temporal development of the soot mass can be evaluated. The soot mass production rate is calculated as the temporal differential of the total soot mass development during the premixed burn phase.

Soot Gradient

The soot gradient is defined as the soot mass per unit length along the spray axis, as illustrated in Figure 5. This is calculated from the cross-sectionally integrated KL distribution.

As seen in Figure 5, the liquid core overlaps with the soot producing region of the spray, making this region ambiguous. In order to eliminate the liquid core from the integrated KL, the liquid core is estimated by fitting a gaussian profile to the upstream part of the spray, where no soot is expected to form. The downstream part of the liquid core is then estimated based on the upstream line fit. This procedure was verified by applying the same algorithm to a liquid core prior to formation of soot, resulting in a good prediction of the downstream part of the liquid core. The KL distribution from the liquid core was then subtracted from the integrated KL, resulting in the integrated KL caused only by the presence of soot. By applying Equation 7 to the integrated KL, the soot mass distribution along the spray axis was calculated. The soot gradient was calculated as the slope of a linear fit to the soot mass distribution along the spray axis in $\mu g/cm$.

The soot gradient gives a direct measure of the soot production tendency in the quasi steady spray flame. Most of the soot is produced in the central core of the flame where there is a constant competition between soot formation and soot oxidation processes. After the flame lift-off location, soot formation processes dominates over soot oxidation, resulting in an increase of the soot concentration when moving downstream. At a certain point, soot oxidation overtakes soot formation, and the peak soot level is reached. Further downstream, oxidation is dominant and the soot level decays. The soot gradient observed between soot lift-off length position and peak soot position gives a measure of the imbalance between soot oxidation and soot formation.

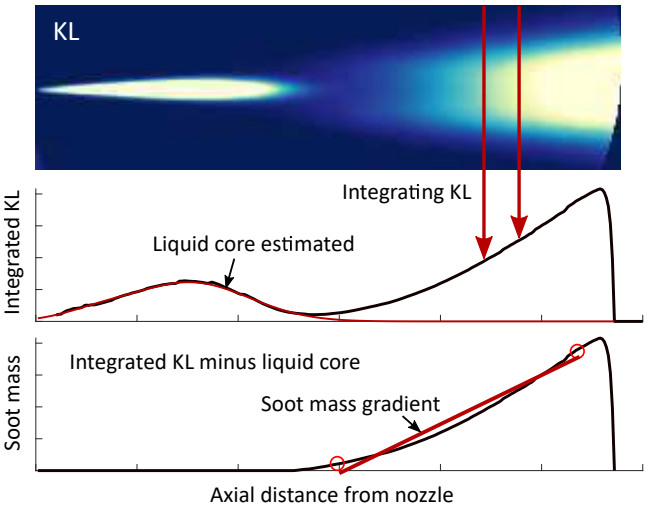

Figure 5: Illustration of how the soot gradient is calculated. Top image: KL distribution; middle image: cross-sectionally integrated KL values along the spray axis, estimated liquid core contribution is displayed in red; bottom image: the resulting soot mass distribution after subtracting the liquid core from the integrated KL.

Temporal Analysis of Soot and FLOL

In order to investigate the instantaneous effect of FLOL on in-flame soot, the FLOL was also determined temporally. This was achieved by plotting the OH* chemiluminescence along the central spray axis temporally, see Figure 6. The x-axis is time after start of injection (ASOI), whilst y-axis is the distance from the nozzle hole along the central spray axis, giving a temporal overview of the FLOL behavior. This type of plot is also known as an I-x-t plot, displaying an intensity distribution in the axial position/time plane. An interesting feature that can be observed in the plots are the tilted streaks, which display the convection of turbulent structures along the central axis. If assuming that the turbulent structures follows the spray bulk motion, this provides an estimation of the spray velocity. This information will be used in the interpretation of the interaction between soot production and equivalence ratio at flame lift-off location.

Similar to the representation of the temporal development of the OH*, a temporal representation of soot is given. However, instead of tak-

ing the values along the spray central axis, the cross-sectionally integrated KL values are calculated. In this way, the total soot mass in each pixel-wide slice volume of the spray is plotted along the y-axis of Figure 6, resulting in the temporal development of the axial distribution of soot mass in the reacting spray.

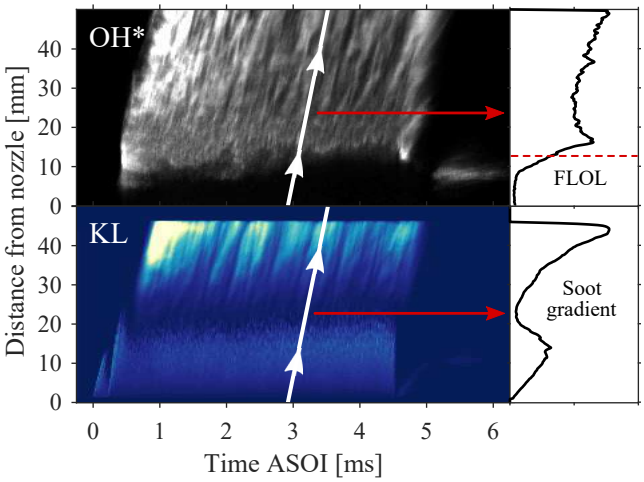

Figure 6: Temporal representation of cross-sectionally integrated KL and OH* along the spray axis. The line plots on the right hand side represent the values along the "tilted" white lines. Values along the white line represent the trajectory of a gas parcel traveling in the spray. Lighter color means higher values of OH* and integrated KL.

Due to the highly transient behavior of the FLOL, the amount of air mixed in with the spray prior to FLOL varies accordingly. This transient behavior translates into a fluctuating in-flame soot production, where a gas parcel traveling from the flame lift-off location with a certain equivalence ratio, will have a soot production accordingly as it moves downstream. In order to relate the instantaneous equivalence ratio at FLOL to the corresponding soot production, values along a "tilted" line in Figure 6 are extracted. The line is "tilted" according to the estimated spray velocity, as mentioned previously. This results in extracting information from a gas parcel traveling along the spray axis. The calculated soot gradient and the FLOL are based on the average of 10 consecutive trajectories ("tilted" lines). This method was found to give more correlating results with regards to the relation between $\bar{\phi}(H)$ and the soot production. By comparing the temporal soot gradient to the corresponding equivalence ratio at the FLOL, the interaction between air entrainment and soot production for all the fuels and conditions can be assessed, eliminating the uncertainty resulting from having an unsteady FLOL.

Results and Discussion

Combustion Characteristics

In this section, combustion characteristics are presented. This includes the calculated apparent heat release rate (aHRR) and IDTs.

The apparent heat release rate (aHRR) was calculated from the in-cylinder combustion pressure based on a first law approach described by Heywood[47] and is shown in Figure 7, top row. The bottom row of Figure 7, shows the sum of all pixel values captured by the OH* chemiluminescence high speed measurement, where the OH*-based IDT is defined as the time between start of injection and the first observed OH* signal.

The aHRR curves of all fuels have similar characteristics. When considering each condition separately, ignition starts at similar timings and a premixed burn phase is evident for all fuels. The magnitude of the premixed burn phase is correlated with the IDTs, for a longer IDT, a larger release rate is observed. This is due to having a longer period for fuel and air to mix prior to ignition, leading to a larger portion of the injected fuel to burn as a premixed flame. After the premixed burn phase the mixing-controlled burn phase occurs. This phase is unaffected by the IDT, and seen to be very similar in magnitude and shape for all fuels and conditions. This phase will from here on be referred to as the quasi-steady period.

The IDTs are expected to follow the cetane number rating of the fuels. In general, longer chain lengths and a lower degree of unsaturation results in higher cetane numbers.[26] As seen in Table 4, two cetane numbers are given, cetane number and derived cetane num-

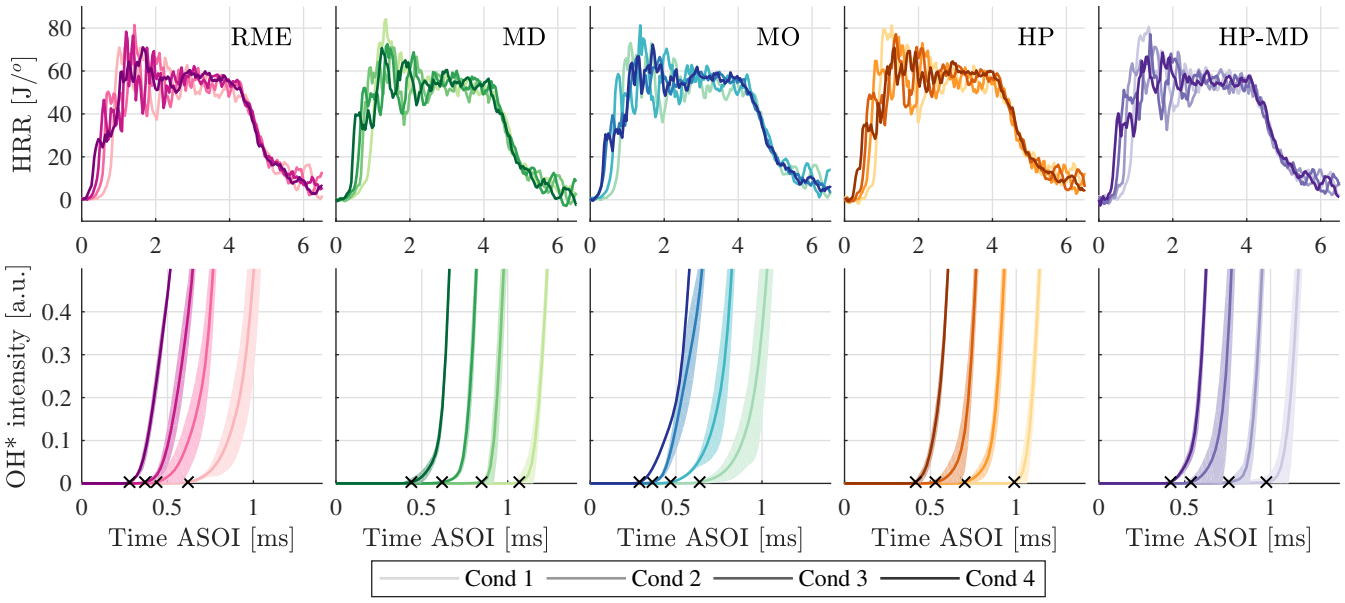

Figure 7: Apparent heat release rate (top row) and the total OH* chemiluminescence intensity for all fuels and conditions tested (bottom row). The occurrence of first OH* chemiluminescence signal is indicated with a cross. The HRR and OH* intensity shown are ensemble averaged and the bands indicate the ±1 standard deviation.

ber (DCN). The trends of the two are slightly different. When considering the cetane number, RME, MO and heptane have similar values of ∼57, whilst MD has the lowest value of ∼48. This suggests that RME, MO and heptane should have the shortest IDTs. As seen in Figure 8, this is not case in the current study, where RME and MO have similar IDTs, and MD and heptane have longer IDTs.

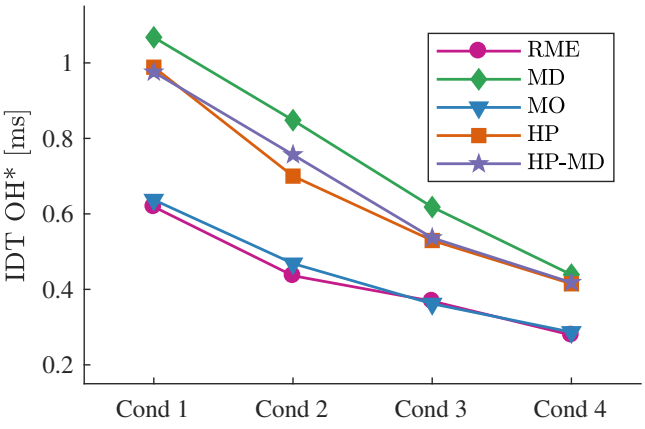

Figure 8: OH*-based IDTs, and is determined from the first occurrence of the ensemble averaged OH* signal.

When considering the DCNs of the fuels, the results are more correlated, MD and heptane have DCNs of 51.6 and 53 respectively, whilst RME and MO have ∼59. The reason for the DCNs being more correlated to the current results is likely to be due to the different operating conditions used when determining the DCN with the IQT™ and the cetane number with the CFR engine. With the device IQT™, a single ambient gas condition is chosen, whilst the CFR engine uses a range. Because of the poorer low temperature ignition properties of MD,[10] a lower cetane number is measured compared to heptane. The DCN is therefore more representative for the conditions used in the current study.

Flame Lift-off Length

The FLOL for all fuels and conditions were determined from the OH* chemiluminescence images. A sample size of 30 combustion cycles were used to get a representative mean. Figure 9 shows the mean temporal behavior of the FLOL plotted together with a ±1 standard deviation band to indicate the uncertainty. The FLOL has a tendency of starting with larger values, especially for the lower ambient temperature conditions, and stabilizing at a shorter

distance later in the cycle. A possible contributor to this could be colder ambient gas temperatures before combustion. As combustion occurs, the ambient gases are further compressed by the combustion pressure rise, increasing the temperature. This is also likely to be the cause of the unstable lift-off length seen in the chamber, since the combustion process is a highly stochastic event. This effect is much stronger in a small volume combustion chamber such as the current one, whilst less evident in a typical constant volume combustion chamber, where the chamber volume is much larger. The FLOL stabilizes between 3 and 4 ms ASOI, which is also used as the quasi-steady period of the combustion period. Towards the end of the period, the FLOL observed to increase slightly. This might be due to the ambient gas temperature decrease in the expansion stroke (see Figure 2). For MD during the coldest condition, the FLOL did not stabilize before ∼1.5 ms ASOI.

The average values of the FLOL during the quasi-steady period for all conditions and fuels are shown in the Figure 10. All fuels show a monotonically decreasing trend with increasing ambient gas temperatures. RME has the shortest FLOL for all conditions, followed by MO. The short chain molecule group of HP, MD and HP-MD have quite similar FLOLs for all conditions, except the coldest one, where MD has a longer average FLOL. The FLOL has in some cases been shown to correlate closely with the cetane number,[48] although this is not always true, especially for oxygenated fuels,[10] where the fuel-bound oxygen can affect the laminar flame speed and the location of the stoichiometric mixture fraction contour. When comparing the FLOL with the measured OH*-based IDTs, a clear correlation can be made, see Figure 11. For shorter IDTs, shorter FLOLs are observed, vice versa. However, MD can be seen to deviate from the correlation for the coldest condition, where the FLOL is longer than what the trend would suggest.

Sooting Characteristics

Ensemble Averaged KL

Ensemble averaged KL images for all fuels and conditions tested are shown in Figure 12. The individual steady images are constructed from a total of 2730 images taken during the quasi-steady period.

As seen in Figure 12, all turbulent structures in the spray are averaged out, displaying only the mean behavior. The liquid core of the spray can be seen, where the trend of the liquid length closely follows the inverse of the volatility of the fuels, i.e. RME>MO>MD>HP-MD>HP. Downstream of the liquid core, soot is observed. The amount of soot produced in the spray increases when moving downstream. As mentioned previously, the peak soot level is located outside the measurement domain and therefore not captured in these measurements.

Looking at each fuel individually, the liquid length can be seen to decrease as ambient gas temperature increases. This is due to the hotter ambient gas vaporizing the liquid droplets faster. It is also clear that soot production in the spray flame increases as the ambient gas temperature increases. This is a consequence of the equivalence ratio at flame lift-off location, which was presented in the previous section. A higher ambient gas temperature results in a shorter FLOL and consequently less air is entrained into the spray upstream of the FLOL. As the fuel-rich mixture has enough residence time, ignition starts and products are formed. A richer mixture prior to ignition leads to production of more soot precursors downstream of FLOL, such as polycyclic aromatic hydrocarbons (PAH), benzene and acetylene.[49] From the gaseous soot precursors, soot nuclei are formed, surface growth and agglomeration occurs, resulting in a large enough concentration of soot particles to be captured by the measurement technique.

Soot production in a turbulent non-premixed flame is mainly governed by air entrainment upstream of FLOL and fuel effects. In order to investigate the fuels' effect on soot production, Figure 13 shows the soot gradient from the steady KL measurement plotted against the

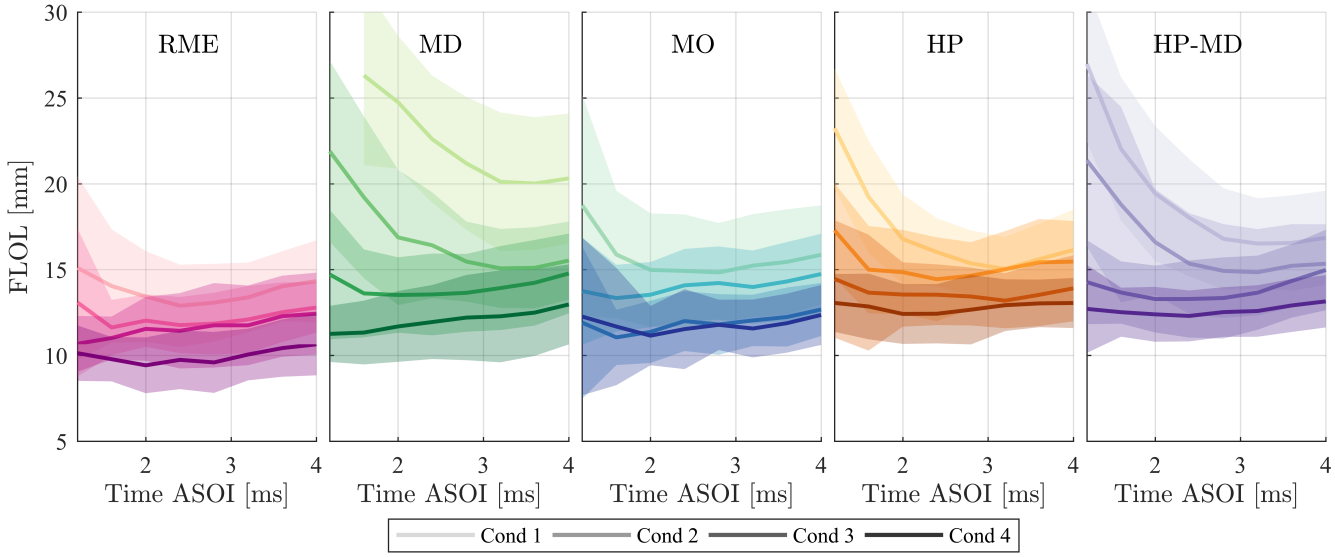

Figure 9: Ensemble averaged temporal development of the flame lift-off length, including the ±1 standard deviation.

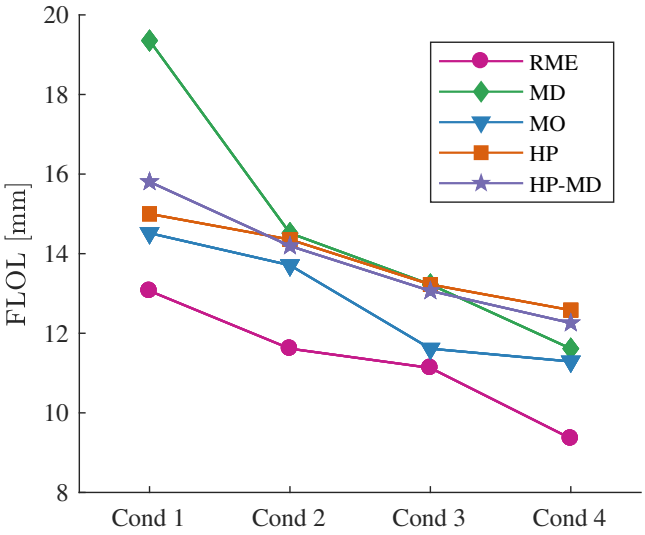

Figure 10: Average FLOLs during the quasi-steady period.

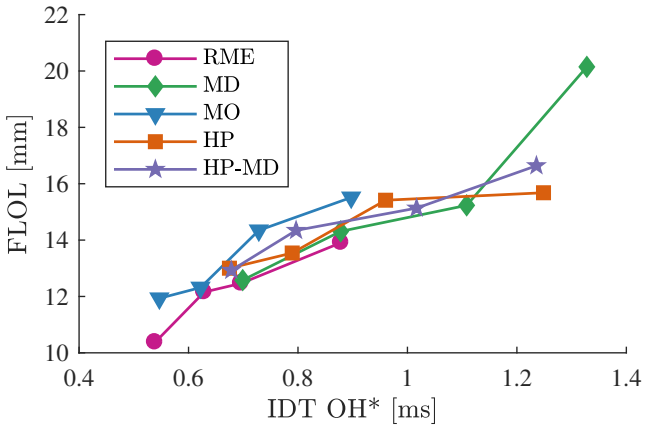

Figure 11: Comparison between OH*-based IDT and FLOL.

equivalence ratio at FLOL ($\bar{\phi}(H)$). In this plot, one can compare the soot production in the flame for constant equivalence ratios at FLOL, and fuel effects can be singled out. The results show that MD has the lowest soot production, whilst the longer chain esters have the highest. Heptane has a slightly lower soot production than the long chain esters. For all equivalence ratios estimated, the ordering of soot production is RME>MO>HP>HP-MD>MD. Fuel effects on soot production will be discussed later in this section.

Temporal Distribution of OH* Chemiluminescence and KL

The temporal development of the OH* chemiluminescence and KL during the premixed burn phase for the hottest condition are discussed. Figure 14 shows the temporally ensemble-averaged measurement for the time interval 0.08 ms to 0.48 ms after start of OH* ignition. Each image is an average of 30 measurements.

In Figure 14, ignition starts for all fuels close to the nozzle tip. For RME and MO, the ignition starts closer to the nozzle than for the other fuels, this is likely due to the later ignition of the short chain fuels, resulting in the igniting part of the fuel-air mixture to move further down-

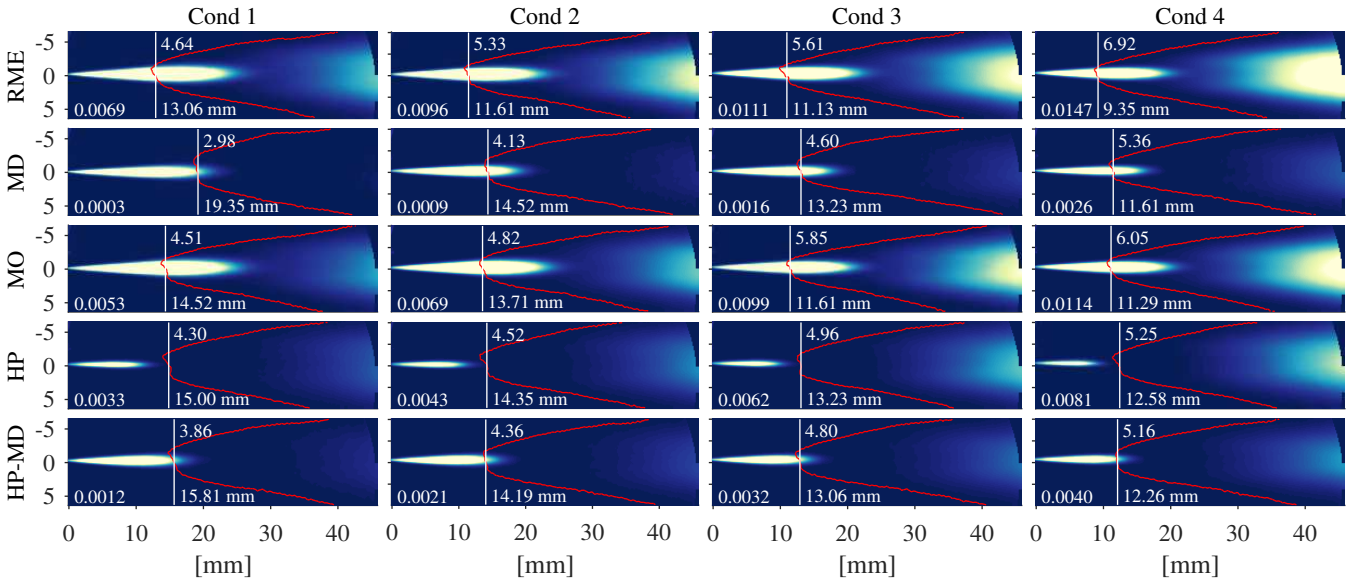

Figure 12: Ensemble averaged KL plots, where the KL scale ranges from 0 to 1.4. The white line indicates the FLOL. The red contour indicates the location of the 50% OH* shoulder value. The soot gradient in $\mu g/cm$ is indicated in the bottom left corner, the equivalence ratio at FLOL is indicated in the top middle and the FLOL in mm is indicated in the bottom middle.

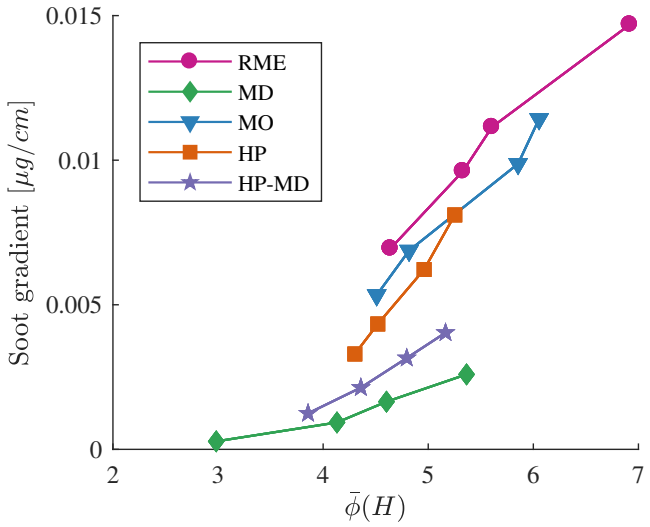

Figure 13: Equivalence ratio at FLOL plotted against soot gradient from the ensemble averaged data.

stream for the short chain fuels compared to the long chain fuels. The initial ignition kernel close to the nozzle tip observed here is different from that observed in constant volume vessels,[48] where ignition starts at or downstream of the stabilized flame lift-off location. The observed upstream ignition kernel is likely caused by injector specifics. The spray penetration velocity is observed to be slower in the beginning and increasing later on. This results in some fuel being present closer to the nozzle, igniting upstream of the stabilized FLOL. This will of course affect the premixed phase and must be taken into account when comparing to simulations. For the long chain fuels, the initial flame propagates from the near nozzle ignition kernel towards the tip of the spray. While for the short chain fuels, a new ignition kernel is formed in the downstream part of the spray around 0.6-0.7 ms ASOI, where fuel and air have had time form a premixed mixture. The two ignition kernels are later joined together, resulting in having similar characteristics compared to the long chain fuels. This is also observed in the aHRR in Figure 7, where the short chain fuels have higher heat release rate during the premixed burn phase than the long chain fuels.

RME and MO have very similar temporal OH* characteristics, which is expected since RME consists of 61.8 w% MO. MD and heptane also have relatively similar temporal OH* characteristics, which is more surprising, given that the molecular structure of the two fuels are very different. However, the DCN of the two are similar, suggesting that the ignition properties should be similar.

Figure 15 shows the temporal development of

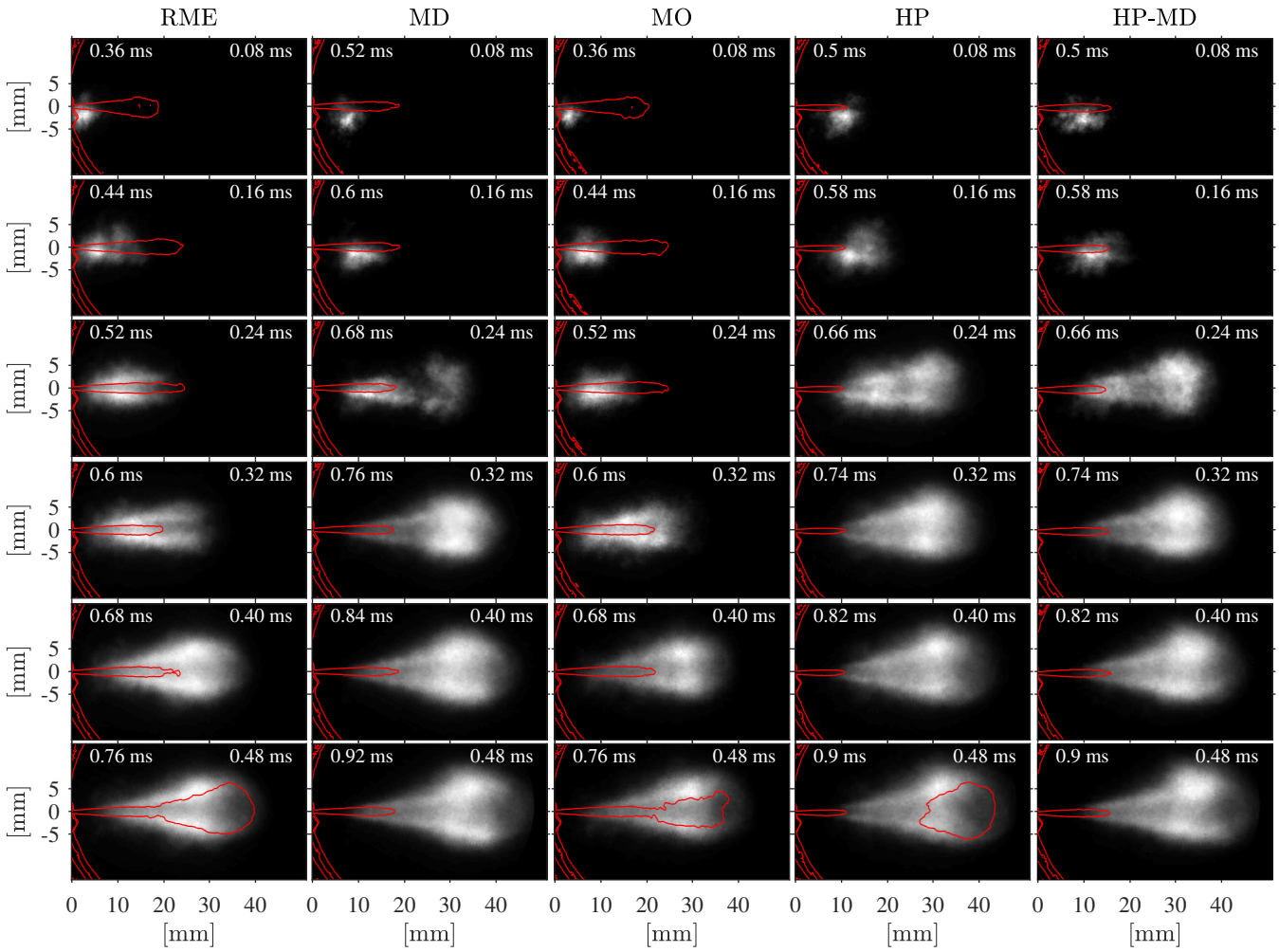

Figure 14: Ensemble averaged plots showing the temporal development of OH* chemiluminescence during the premixed burn phase for the highest ambient gas temperature condition. The red line indicates the contour of the KL measurement. The indicated time on the left is time ASOI and the time on the right is time after start of ignition by OH*.

KL for the time interval 0.4 ms and 0.6 ms after start of OH* ignition. Figure 16 shows the time after OH* ignition at which maximum soot production rate occurs together with the time of inception of soot. As seen in Figure 16, soot starts to form around 0.3 ms and 0.4 ms after start of OH* ignition for the hottest condition, meaning that Figure 15 shows the approximate start of soot production in the first row and the time of maximum soot mass rate in the last row. A general characteristic of the temporal development of soot production in the flame is that the highest soot production rate is found in the head of the spray. For the long chain fuels, soot is first formed close to the end of the liquid core. For the short chain fuels, soot is first formed further downstream. This due to the longer IDT of the short chain fuel, where the spray flame has had time to develop before soot starts to form. Fuel volatility also has an impact on the initial premixing and the IDT, where the short chain fuels, having higher volatility, evaporate faster, resulting in shortening of the IDT.

For increasing ambient gas temperatures in Figure 16, the time of soot inception is advanced, whilst the time of maximum soot production is held relatively stable, especially for the three hottest conditions. This indicates that an increase in ambient gas temperature decreases the time for the first detectable soot particles to form. The time between OH* ignition and maximum soot rate occurrence is relatively unaffected by the temperature increase. The maximum soot production rate for all fu-

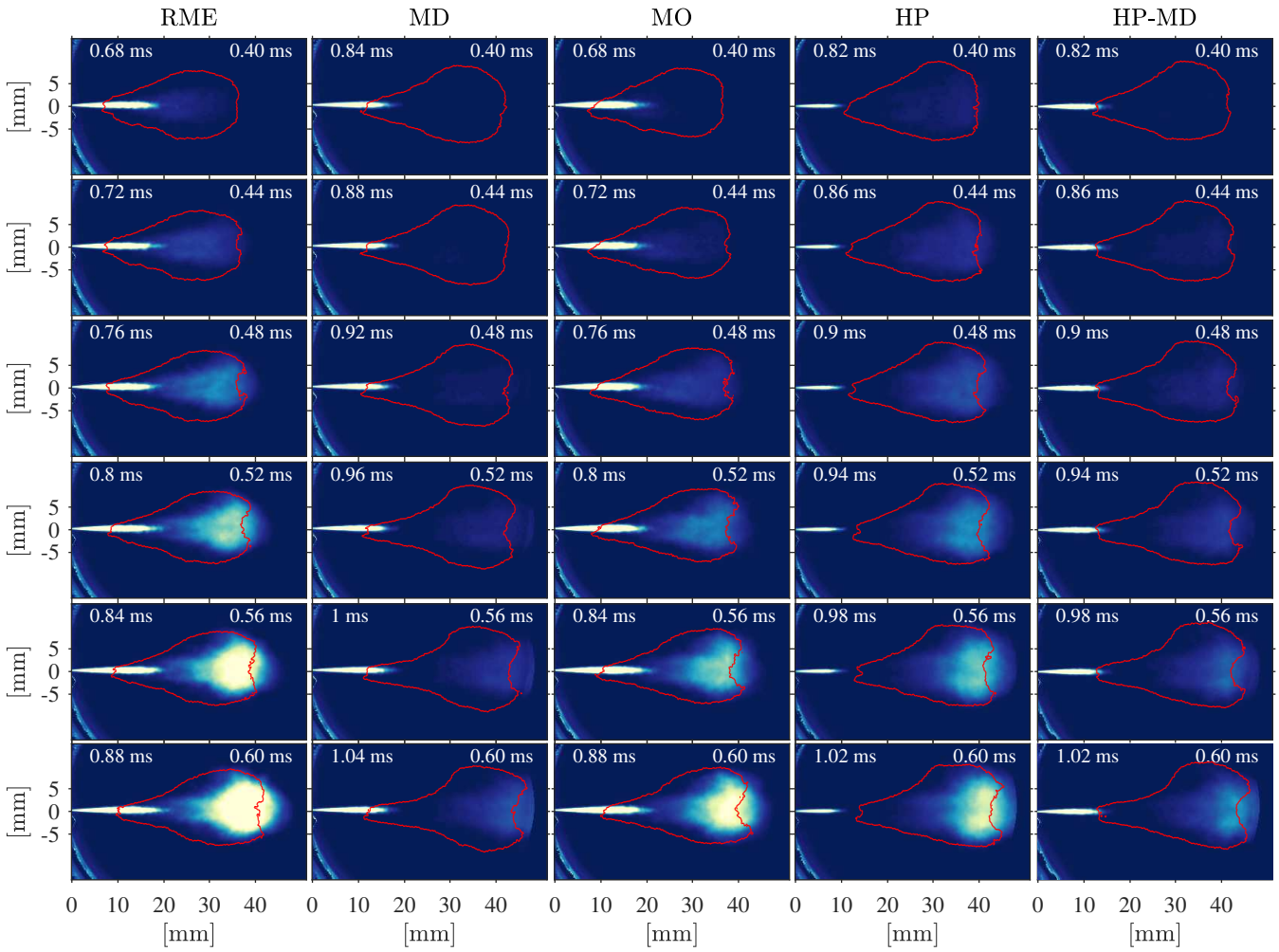

Figure 15: Ensemble averaged plots showing the temporal development of KL during the premixed burn phase for the highest ambient gas temperature condition. The red line indicates the contour of the OH* chemiluminescence measurement. The indicated time on the left is time ASOI and the time on the right is time after start of ignition by OH*.

els and conditions are shown in Figure 17. The data for condition 3 and 4 are most representative of the total soot produced because of the early ignition resulting in the initial soot being produced within the measurement domain. The maximum soot production rate increases for higher ambient gas temperatures, and has the same ordering as the soot gradient during quasi-steady period, i.e. RME>MO>HP>HP-MD>MD.

Instantaneous Soot Production and Local Equivalence Ratio

An analysis of the instantaneous $\bar{\phi}(H)$ and the instantaneous soot gradient was performed based on their temporal development and is shown in Figure 18. In these plots, the instantaneous equivalence ratio at FLOL and the corresponding soot gradient are plotted temporally over the combustion period. This approach minimizes the effects of an unstable FLOL on the soot production since temporal effects are captured. Each point in Figure 18 represents an instantaneous measurement during an injection event, not considering the early and late phases of the combustion period, approximately between 1 ms and 4 ms ASOI. The plots on top and to the right of each figure indicate the number density of the points along their respective axes, showing each condition separately. From this, the spread in the results of measured $\bar{\phi}(H)$ and soot gradient is observed. The $\bar{\phi}(H)$ and the soot gradient have a relatively

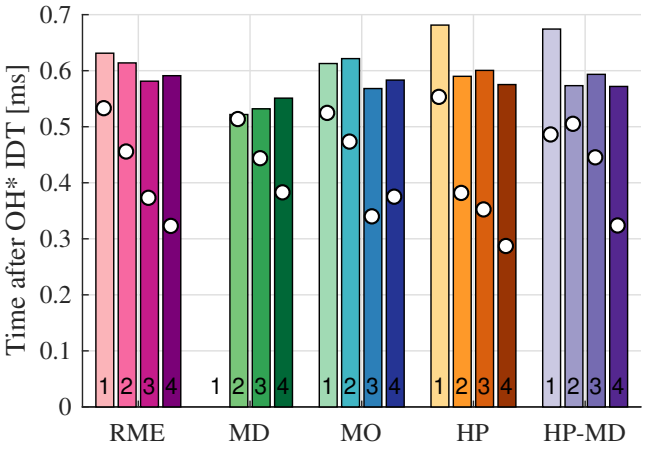

Figure 16: Time between OH*-based ignition and max production rate of soot. The time of inception of soot is indicated as white circles and the numbers at the bottom indicate the condition. No soot was detected for MD at condition 1.

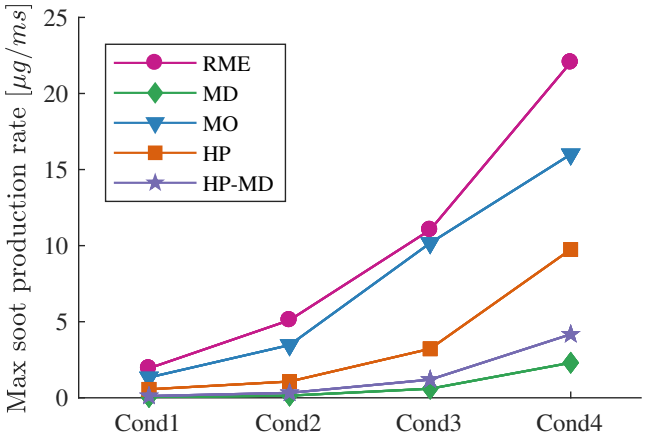

Figure 17: Maximum soot production rate.

large spread, indicating that the combustion is highly stochastic. However, the $\bar{\phi}(H)$ and the soot gradient correlate quite well, even within a single condition, where a low equivalence ratio at FLOL leads to a lower soot gradient and vice versa.

For equivalence ratio values below approximately 2, no soot is expected to be formed, as concluded by Pickett and Siebers,[15] which can be observed in the current measurements. All fuels starts forming soot between approximately $\bar{\phi}(H) = 2$ and 2.5. As seen in Equation 5, the fuel-bound oxygen is taken into account when calculating $\bar{\phi}(H)$, making Figure 18 mostly dependent on fuel molecular and ambient gas temperature differences.

An interesting observation can be seen when investigating the scatter plot for an individual fuel. If the soot gradient was independent of the ambient gas temperature increase between the conditions, the condition-wise trend lines of the points would be expected to overlap each other as the equivalence ratio increased. However, when calculating a least-square linear fit for each condition, the lines for each condition do not line up. This means that for the same equivalence ratio, the soot gradient increases for increasing ambient gas temperatures, indicating that there is a clear effect of temperature on soot production for all fuels. This was also observed in Ref. 41 and Ref. 50.

Discussion on Fuel Effects on Soot Production

The difference in soot production between RME and MO is interesting, since these two fuels are very similar in composition. In Table 4, the main difference between RME and MO is the degree of unsaturation. RME has a 10% higher degree of unsaturation compared to MO. The degree of unsaturation in esters has been shown in several studies to increase the sooting tendency of a non-premixed flame.[22,51,52] The higher degree of unsaturation in the RME can then likely explain the higher soot production seen in these measurements.

When comparing the properties of MD and heptane, many differences can be pointed out. MD has a higher number of C-C bonds and a higher degree of unsaturation, which both promotes the production of soot precursors. In addition, MD has an ester moiety and a high content of oxygen in the molecule, which previously has shown to reduce soot production compared to a similar chain length alkanes.[52] Since a lower soot production is observed in the measurements, it is evident that the presence of the ester functional group and the fuel-bound oxygen in MD are the dominating effects in the reduction of soot production.

The 50 % molar blend of heptane and MD (HP-MD) resulted in a soot production that was in between heptane and MD. This is expected since the properties determining the soot

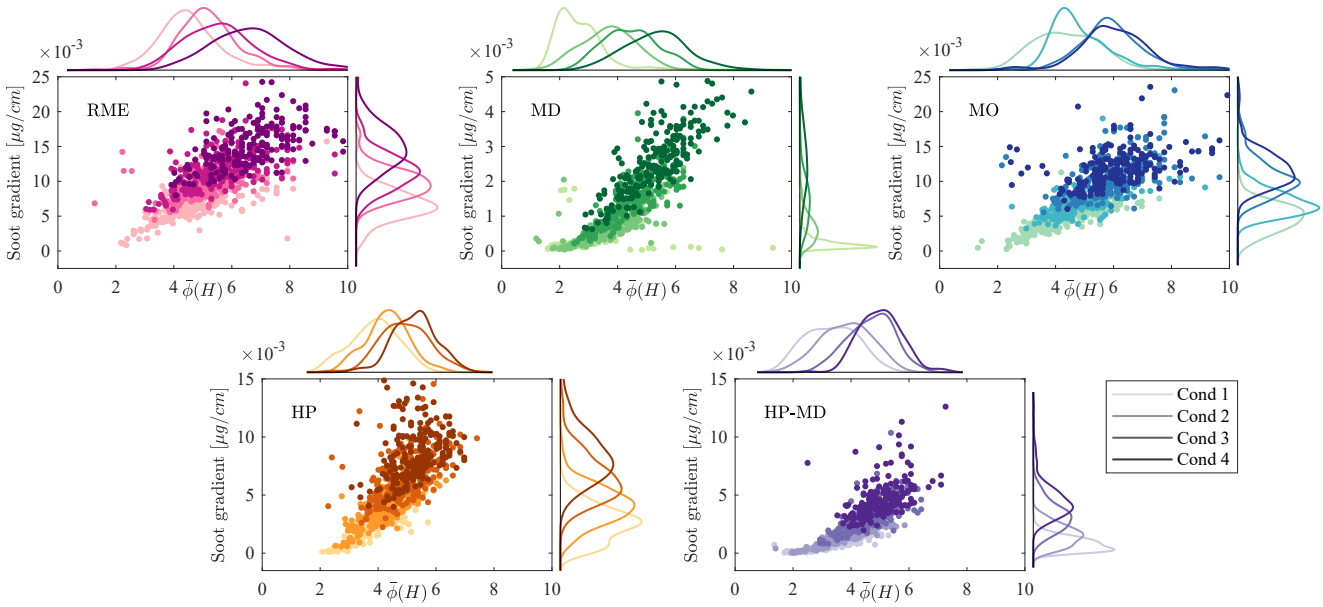

Figure 18: Instantaneous soot gradient versus equivalence ratio plots.

production are based on molecular properties, the 50 % molar blend yields the mean of the important properties listed above.

Temperature effects on the soot gradient in Figure 13 must be taken into account when comparing the fuels. For instance, when considering soot gradients for all fuels at $\bar{\phi}(H) = 4.5$, the ambient gas temperatures for each fuel at this equivalence ratio are different, since the points for each fuel in the plot represents different conditions. At $\bar{\phi}(H) = 4.5$ MD is close to condition 3, heptane is close to condition 2, RME/MO are close to condition 1. This temperature effect can however be eliminated by plotting the individual conditions at the time, shown in Figure 19 for condition 4. The variation of the equivalence ratio is here only due to the change in FLOL under the same ambient gas temperature, showing that the temperature effect on soot production does not change the soot gradient ordering for a given equivalence ratio.

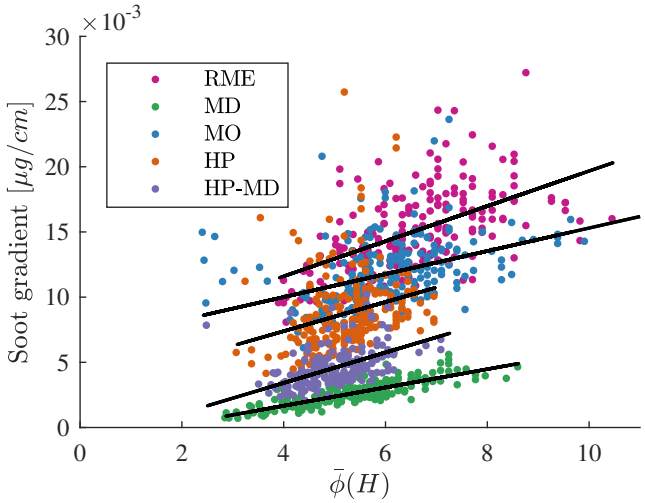

Figure 19: Instantaneous $\bar{\phi}(H)$ and the soot gradient for the hottest condition, the lines show the least square linear fit of the individual fuels.

Conclusions

Detailed measurements of in-flame soot and FLOL of compression-ignited flames of fuels relevant for biodiesel combustion have been conducted. The main conclusions are listed below.

- The fuels can be split into two groups, short and long carbon-chain fuels. The long chain fuels, i.e. RME and neat MO, was observed to have shorter IDTs com-

pared to the short chain fuels (MD and heptane). Consequently, a higher heat release rate during the premixed combustion phase was observed for the short chain fuels, due to more premixing prior to start of ignition.

- The FLOL correlated well with the ignition properties of all fuels, except for methyl decanoate, for the coldest condition, where the FLOL was found to deviate from the general trend.

- For a constant equivalence ratio at the flame lift-off location, the order of in-flame soot production was found to be RME>MO>HP>HP-MD>MD. The higher sooting tendency of RME compared to MO is likely due the higher degree of unsaturation. While the lower sooting tendency of MD compared to heptane was mainly attributed to the high fuel oxygen ratio.

- Extrapolating the in-flame soot production for equivalence ratios at FLOL leaner than 2-2.5 yielded sootless combustion for all fuels tested.

- The instantaneous soot production in the spray and the corresponding equivalence ratio at FLOL correlated well within each individual combustion period, supporting the argument of air entrainment prior to FLOL being a very important factor for in-flame soot production.

- From analyzing the instantaneous soot production gradient versus instantaneous equivalence ratio at flame lift-off location over individual injection events, a clear temperature dependence on the balance between soot formation and oxidation was observed. Flames combusting with higher ambient gas temperatures with the same equivalence ratio at FLOL, have higher soot production, meaning that the soot formation rate increases more than the soot oxidation rate for elevated temperatures within the tested temperature range.

- During the premixed combustion phase, soot mass production rate was measured, seeing that the soot mass rate increases substantially as ambient gas temperature is increased. This was likely attributed to the higher equivalence ratio in the fuel-air mixture for the hotter conditions, because of shorter IDTs.

- The IDT between RME and MO was found to be very similar for all conditions, suggesting that the equivalence ratio in the fuel-air mixture prior to the premixed combustion phase was very similar. The $\sim$33% higher maximum soot production rate of RME compared to MO therefore supports the finding of the RME having a higher sooting tendency.

- The time between start of ignition and onset of soot was found to decrease as ambient gas temperature increased. For the three hottest conditions, the time between start of ignition and occurrence of maximum soot mass rate was almost constant for all fuels except for MD. This indicated that the time between onset of soot and occurrence of maximum soot mass rate increases as temperature increases.

Acknowledgement The experiments were conducted in the Motorlab at the Norwegian University of Science and Technology in Trondheim, Norway. The laboratory is supported by the research center Bio4fuels, which is part of Centers for Environment-friendly Energy Research (FME) funded by the Norwegian Research Council.

Supporting Information Available

References

(1) Skeen, S. A. et al. A Progress Review on Soot Experiments and Modeling in the Engine Combustion Network (ECN). *SAE*

International Journal of Engines **2016**, *9*, 883–898.

(2) International Energy Agency, *Renewables 2018*; 2018.

(3) Omidvarborna, H.; Kumar, A.; Kim, D.-S. Recent Studies on Soot Modeling for Diesel Combustion. *Renewable and Sustainable Energy Reviews* **2015**, *48*, 635–647.

(4) Fisher, E.; Pitz, W.; Curran, H.; Westbrook, C. Detailed Chemical Kinetic Mechanisms for Combustion of Oxygenated Fuels. *Proceedings of the Combustion Institute* **2000**, *28*, 1579–1586.

(5) Vaughn, T.; Hammill, M.; Harris, M.; Marchese, A. J. Ignition Delay of Bio-Ester Fuel Droplets. SAE Technical Paper Series. 2006.

(6) Herbinet, O.; Pitz, W. J.; Westbrook, C. K. Detailed Chemical Kinetic Oxidation Mechanism for a Biodiesel Surrogate. *Combustion and Flame* **2008**, *154*, 507–528.

(7) Herbinet, O.; Pitz, W. J.; Westbrook, C. K. Detailed Chemical Kinetic Mechanism for the Oxidation of Biodiesel Fuels Blend Surrogate. *Combustion and Flame* **2010**, *157*, 893–908.

(8) Dagaut, P.; Gaïl, S.; Sahasrabudhe, M. Rapeseed Oil Methyl Ester Oxidation Over Extended Ranges of Pressure, Temperature, and Equivalence Ratio: Experimental and Modeling Kinetic Study. *Proceedings of the Combustion Institute* **2007**, *31*, 2955–2961.

(9) Westbrook, C.; Naik, C.; Herbinet, O.; Pitz, W.; Mehl, M.; Sarathy, S.; Curran, H. Detailed Chemical Kinetic Reaction Mechanisms for Soy and Rapeseed Biodiesel Fuels. *Combustion and Flame* **2011**, *158*, 742–755.

(10) Manin, J.; Skeen, S.; Pickett, L.; Kurtz, E.; Anderson, J. E. Effects of Oxygenated Fuels on Combustion and Soot Formation/Oxidation Processes. *SAE International Journal of Fuels and Lubricants* **2014**, *7*, 704–717.

(11) Cheng, A. S. E.; Dumitrescu, C. E.; Mueller, C. J. Investigation of Methyl Decanoate Combustion in an Optical Direct-Injection Diesel Engine. *Energy & Fuels* **2014**, *28*, 7689–7700.

(12) Dumitrescu, C. E.; Cheng, A. S.; Kurtz, E.; Mueller, C. J. A Comparison of Methyl Decanoate and Tripropylene Glycol Monomethyl Ether for Soot-Free Combustion in an Optical Direct-Injection Diesel Engine. *Journal of Energy Resources Technology* **2017**, *139*, 042210.

(13) Le, M. K.; Zhang, R.; Rao, L.; Kook, S.; Hawkes, E. R. The Development of Hydroxyl and Soot in a Methyl Decanoate-Fuelled Automotive-Size Optical Diesel Engine. *Fuel* **2016**, *166*, 320–332.

(14) Su, H. C.; Kook, S.; Chan, Q. N.; Hawkes, E. R.; Le, M. K.; Ikeda, Y. A Comparison of High-Temperature Reaction and Soot Processes of Conventional Diesel and Methyl Decanoate. *Fuel* **2018**, *226*, 635–643.

(15) Pickett, L. M.; Siebers, D. L. Non-Sooting, Low Flame Temperature Mixing-Controlled DI Diesel Combustion. SAE Technical Paper Series. 2004.

(16) Pickett, L. M.; Siebers, D. L. Fuel Effects on Soot Processes of Fuel Jets at DI Diesel Conditions. SAE Technical Paper Series. 2003.

(17) Park, W.; Park, S.; Reitz, R. D.; Kurtz, E. The Effect of Oxygenated Fuel Properties on Diesel Spray Combustion and Soot Formation. *Combustion and Flame* **2017**, *180*, 276–283.

(18) Zhang, R.; Pham, P. X.; Kook, S.; Masri, A. R. Influence of Biodiesel Carbon

Chain Length on in-Cylinder Soot Processes in a Small Bore Optical Diesel Engine. *Fuel* **2019**, *235*, 1184–1194.

(19) Woschni, G. A Universally Applicable Equation for the Instantaneous Heat Transfer Coefficient in the Internal Combustion Engine. SAE Technical Paper Series. 1967.

(20) Knothe, G. Dependence of Biodiesel Fuel Properties on the Structure of Fatty Acid Alkyl Esters. *Fuel Processing Technology* **2005**, *86*, 1059–1070.

(21) Mueller, C. J.; Pitz, W. J.; Pickett, L. M.; Martin, G. C.; Siebers, D. L.; Westbrook, C. K. Effects of Oxygenates on Soot Processes in DI Diesel Engines: Experiments and Numerical Simulations. SAE Technical Paper Series. 2003.

(22) Sarathy, S.; Gaïl, S.; Syed, S.; Thomson, M.; Dagaut, P. A Comparison of Saturated and Unsaturated C4 Fatty Acid Methyl Esters in an Opposed Flow Diffusion Flame and a Jet Stirred Reactor. *Proceedings of the Combustion Institute* **2007**, *31*, 1015–1022.

(23) Yuan, W.; Hansen, A.; Zhang, Q. Vapor Pressure and Normal Boiling Point Predictions for Pure Methyl Esters and Biodiesel Fuels. *Fuel* **2005**, *84*, 943–950.

(24) Knothe, G. A Comprehensive Evaluation of the Cetane Numbers of Fatty Acid Methyl Esters. *Fuel* **2014**, *119*, 6–13.

(25) Murphy, M. J.; Taylor, J. D.; McCormick, R. L. *Compendium of Experimental Cetane Number Data*; 2004.

(26) Knothe, G., Krahl, J., Van Gerpen, J. H., Eds. *The Biodiesel Handbook*, 2nd ed.; Elsevier: Urbana, Ill, 2015.

(27) Knothe, G. "Designer" Biodiesel: Optimizing Fatty Ester Composition to Improve Fuel Properties. *Energy & Fuels* **2008**, *22*, 1358–1364.

(28) Lemmon, E. W.; McLinden, M. O.; Friend, D. G. *NIST Chemistry WebBook, NIST Standard Reference Database Number 69*.

(29) Beattie, J. A.; Kay, W. C. The Normal Boiling Point and Critical Constants of Normal Heptane. *Journal of the American Chemical Society* **1937**, *59*, 1586–1587.

(30) Yang, C.; Xu, W.; Ma, P. Thermodynamic Properties of Binary Mixtures of *p*-Xylene with Cyclohexane, Heptane, Octane, and *N*-Methyl-2-pyrrolidone at Several Temperatures. *Journal of Chemical & Engineering Data* **2004**, *49*, 1794–1801.

(31) Knothe, G.; Matheaus, A. C.; Ryan III, T. W. Cetane Numbers of Branched and Straight-Chain Fatty Esters Determined in an Ignition Quality Tester Quality Tester. **2003**, 5.

(32) Lilik, G. K.; Boehman, A. L. Effects of Fuel Ignition Quality on Critical Equivalence Ratio for Autoignition. *Energy & Fuels* **2013**, *27*, 1586–1600.

(33) Bohren, C. F.; Huffman, D. R. *Absorption and scattering of light by small particles*; John Wiley & Sons, 2008.

(34) Zhao, H.; Ladommatos, N. Optical Diagnostics for Soot and Temperature Measurement in Diesel Engines. *Progress in Energy and Combustion Science* **1998**, *24*, 221–255.

(35) Skeen, S.; Yasutomi, K.; Cenker, E.; Adamson, B.; Hansen, N.; Pickett, L. Standardized Optical Constants for Soot Quantification in High-Pressure Sprays. *SAE International Journal of Engines* **2018**, *11*, 805–816.

(36) Bjørgen, K. O. P.; Emberson, D. R.; Lovas, T. Diffuse Back-Illuminated Extinction Imaging of Soot: Effects of Beam Steering and Flame Luminosity. SAE Technical Paper Series. 2019.

(37) Pastor, J. V.; Garcia-Oliver, J. M.; Novella, R.; Xuan, T. Soot Quantification of Single-Hole Diesel Sprays by Means of Extinction Imaging. *SAE International Journal of Engines* **2015**, *8*, 2068–2077.

(38) Skeen, S. A.; Yasutomi, K. Measuring the Soot Onset Temperature in High-Pressure N-Dodecane Spray Pyrolysis. *Combustion and Flame* **2018**, *188*, 483–487.

(39) Westlye, F. R.; Penney, K.; Ivarsson, A.; Pickett, L. M.; Manin, J.; Skeen, S. A. Diffuse Back-Illumination Setup for High Temporally Resolved Extinction Imaging. *Applied Optics* **2017**, *56*, 5028.

(40) Higgins, B.; Siebers, D. Measurement of the Flame Lift-Off Location on Dl Diesel Sprays Using OH Chemiluminescence. SAE Technical Paper Series. 2001.

(41) Pickett, L. M.; Siebers, D. L. Soot in Diesel Fuel Jets: Effects of Ambient Temperature, Ambient Density, and Injection Pressure. *Combustion and Flame* **2004**, 22.

(42) Naber, J.; Siebers, D. L. Effects of Gas Density and Vaporization on Penetration and Dispersion of Diesel Sprays. SAE Technical Paper Series. 1996.

(43) Siebers, D. L. Scaling Liquid-Phase Fuel Penetration in Diesel Sprays Based on Mixing-Limited Vaporization. SAE Technical Paper Series. 1999.

(44) Siebers, D. L.; Higgins, B.; Pickett, L. Flame Lift-Off on Direct-Injection Diesel Fuel Jets: Oxygen Concentration Effects. SAE Technical Paper Series. 2002.

(45) Totton, T. S.; Chakrabarti, D.; Misquitta, A. J.; Sander, M.; Wales, D. J.; Kraft, M. Modelling the Internal Structure of Nascent Soot Particles. *Combustion and Flame* **2010**, *157*, 909–914.

(46) Choi, M. Y.; Mulholland, G. W.; Hamins, A.; Kashiwagi, T. Comparisons of the Soot Volume Fraction Using Gravimetric and Light Extinction Techniques. *Combustion and Flame* **1995**, *102*, 161–169.

(47) Heywood, J. B. *Internal Combustion Engine Fundamentals*; McGraw-Hill, 1988.

(48) Pickett, L. M.; Siebers, D. L.; Idicheria, C. A. Relationship Between Ignition Processes and the Lift-Off Length of Diesel Fuel Jets. SAE Technical Paper Series. 2005.

(49) Tree, D. R.; Svensson, K. I. Soot Processes in Compression Ignition Engines. *Progress in Energy and Combustion Science* **2007**, *33*, 272–309.

(50) Kook, S.; Pickett, L. M. Effect of Fuel Volatility and Ignition Quality on Combustion and Soot Formation at Fixed Premixing Conditions. *SAE International Journal of Engines* **2009**, *2*, 11–23.

(51) Das, D. D.; McEnally, C. S.; Pfefferle, L. D. Sooting Tendencies of Unsaturated Esters in Nonpremixed Flames. *Combustion and Flame* **2015**, *162*, 1489–1497.

(52) Kholghy, M. R.; Weingarten, J.; Sediako, A. D.; Barba, J.; Lapuerta, M.; Thomson, M. J. Structural Effects of Biodiesel on Soot Formation in a Laminar Coflow Diffusion Flame. *Proceedings of the Combustion Institute* **2017**, *36*, 1321–1328.